

Constraining regional-scale groundwater transport predictions with multiple geophysical techniques

Chris Li^{a,b,*}, Rebecca Doble^a, Michael Hatch^b, Graham Heinson^b, Ben Kay^b

^a CSIRO Land and Water, Urrbrae, South Australia, Australia

^b The University of Adelaide, Adelaide, South Australia, Australia

ARTICLE INFO

Keywords:

Groundwater model
Geophysics
Nuclear magnetic resonance
Electromagnetics
Magnetotellurics
Fractured Rock

ABSTRACT

Study region: The study area is located at Kapunda, South Australia with a semi-arid climate and comprises a fractured rock aquifer. Established in 1842, Kapunda was the first mining town in Australia and its open-pit mine was a key economic driver for the whole continent. The mine was closed in 1879 and the remnant low-grade copper was considered sub-economic, hence the mine has been developed into a tourist attraction. With the recent advances in In-Situ Recovery (ISR), the feasibility of recovering the remnant copper is under consideration again.

Study focus: A field trial involving lixiviant injection and extraction is under development. This study uses a combination of stochastic groundwater modeling and multiple geophysical techniques to investigate (1) the flow paths of injectant and whether it will reach the Light River, and (2) the injectant residence time in the aquifer.

New hydrological insights for the region: Depending on the effective porosity of the aquifer, the modeling suggests a probability of 1 %–5 % for the injectant to escape the site. There is a large uncertainty in the simulated injectant residence time, ranging from 200 to beyond 1000 days. These analyses are conservative and do not consider the biodegradability of the injectant, which can achieve a 90 % degradation over 28 days. Our modeling shows no evidence that the injectant can reach the Light River within this timeframe.

1. Introduction

Numerical modeling is useful for informing management decisions about groundwater resources (Hunt and Zheng, 2012). However, its effectiveness is hampered by various sources of uncertainty, including data, conceptualization and parameterization (Doherty and Simmons, 2013). This is partly because spatial continuity of model parameters is generally assumed to support a more straightforward uncertainty analysis, while most classical hydrogeological techniques provide point-scale information (Brunner et al., 2006). This mismatch can be mitigated by complementing groundwater models with geophysics due to its denser spatial coverage, non-invasiveness and relatively low cost on an area basis (Slater, 2007).

Audio-frequency Magnetotellurics (AMT) and Time-domain Electromagnetics (TEM) are electromagnetic methods that estimate subsurface electrical resistivity, which is related to groundwater salinity, sediment texture, mineralogy and degree of saturation (Everett, 2013). Nuclear Magnetic Resonance (NMR) a geophysical technique that detects subsurface water directly and provides

* Corresponding author at: CSIRO Land and Water, Urrbrae, South Australia, Australia.

E-mail addresses: chris.li@csiro.au, chris_lhy@outlook.com (C. Li), rebecca.doble@csiro.au (R. Doble), michael.hatch@adelaide.edu.au (M. Hatch), graham.heinson@adelaide.edu.au (G. Heinson), ben.kay@adelaide.edu.au (B. Kay).

<https://doi.org/10.1016/j.ejrh.2021.100841>

Received 26 January 2021; Received in revised form 10 April 2021; Accepted 1 June 2021

2214-5818/© 2021 Published by Elsevier B.V. This is an open access article under the CC BY-NC-ND license

(<http://creativecommons.org/licenses/by-nc-nd/4.0/>).

information on pore size distribution and water content, the latter of which is a proxy for porosity in the saturated zone (Legchenko et al., 2002). These geophysical techniques have proven useful in previous studies for constraining important components of groundwater models, including conceptualizations, geological framework and hydraulic properties. For example, Wagner (2007) used AMT to determine the freshwater-saltwater transition zone under Amchitka Island to model the transport of subsurface radioactive materials to the sea floor. Marker et al. (2015) used TEM to improve the hydrostratigraphic characterization for a hydrological model to estimate groundwater levels in Norsminde, Denmark. Boucher et al. (2012) used NMR to estimate transmissivity and specific yield for a groundwater model to assess recharge to a sandstone aquifer in Niger. However, these studies only coupled geophysics with groundwater modeling in a deterministic manner, where a single, best-calibrated groundwater model was developed and used to make predictions. In addition, the uncertainty inherent in geophysical data was rarely quantified and accounted for in groundwater model inversion.

For groundwater model inversion, the Gauss-Levenberg-Marquardt (GLM) algorithm (Hanke, 1997) is commonly used for parameter estimation and uncertainty analysis via programs such as PEST (Doherty et al., 1994), PESTPP (Welter et al., 2015) and UCODE (Poeter et al., 2014). The GLM algorithm requires a sensitivity matrix known as the Jacobian matrix, which is commonly constructed using a finitedifference approach. An alternative approach was proposed by White (2018), who implemented the ensemble-smoother form of the GLM algorithm from Chen and Oliver (2013) into the PESTPP suite, referred to as PESTPP-IES. The ensemble-smoother method derives the Jacobian matrix empirically from an ensemble of random parameter values (White, 2018), which has several advantages. Firstly, it produces an ensemble of calibrated models that can be considered to represent the posterior distribution of parameters and predictions, which can be readily used for non-linear uncertainty analysis and probabilistic predictions. In addition, observation uncertainty can be expressed as a prior variance and used to form a random observation ensemble, allowing the inversion to fit to the observation distribution instead of the observation itself. Furthermore, the ensemble-smoother method decouples the number of parameters being estimated from the number of model runs required, greatly reducing the computational time needed for highly parameterized models (White, 2018).

The objective of this paper is to couple multiple geophysical techniques of AMT, TEM and NMR with stochastic groundwater modelling using the ensemble-smoother framework. We demonstrate how this framework can be used as a data assimilation tool to facilitate the flow of information from geophysical and hydrogeological data to the groundwater model prediction of interest. We also show how the uncertainty of geophysical data can be expressed in a manner that is relevant for groundwater model inversion. This modelling framework was applied in the context of an In-Situ Recovery (ISR) copper mining operation, which involves injecting lixiviant into the ground to dissolve and extract minerals through a system of injection and extraction wells (Sinclair and Thompson,

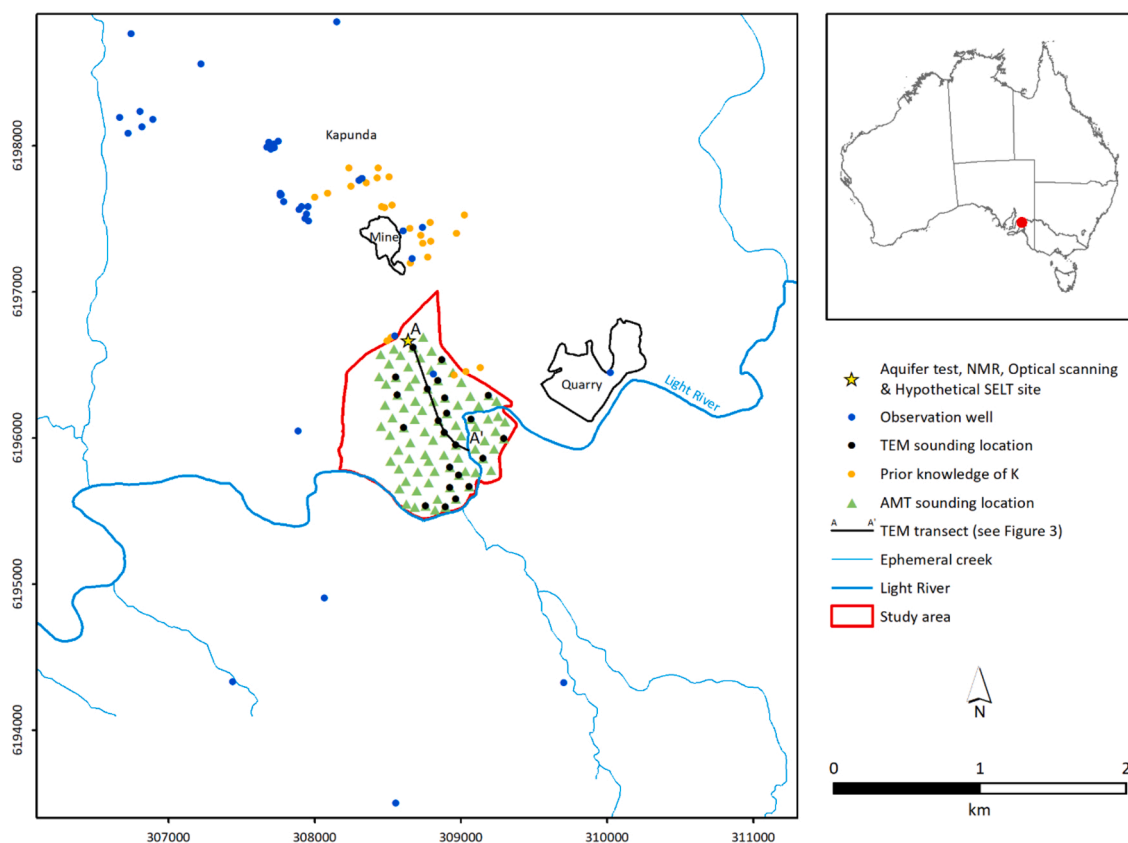


Fig. 1. Kapunda site map, with spatial extent of the groundwater model domain.

2015). The model ensemble was used to predict the regional-scale hydrological impact of a hypothetical ISR trial operation, the results of which are presented in a probabilistic manner.

2. Methods

2.1. Site descriptions

The historical Kapunda copper mine is located approximately 80 km north east of Adelaide, South Australia (Fig. 1). It has a semi-arid climate with a mean annual rainfall of 490 mm/y and evaporation of 1800 mm/y (Bureau of Meteorology, 2020). Established in 1842, Kapunda was the first mining town in Australia and its open-pit mine was a key economic driver for the whole continent until its closure in 1879 (Nirola et al., 2016). The remnant low-grade copper surrounding the mine was considered to be sub-economic, and the mine has since been developed into a heritage site and tourist attraction (Bogenes et al., 2003). With the recent advances in ISR (Sinclair and Thompson, 2015), the feasibility of recovering the remnant copper is under consideration again.

At the time of writing, the proponent is developing a Site Environmental Lixiviant Test (SELT), which is a small-scale operation using a limited number of injection and extraction wells to test various recovery options. The SELT operation is planned to be followed by a remediation phase, where the remaining injectant is retrieved using the extraction well. From a management perspective, the key hydrological issues of concern are: (1) the flow paths of the injectant and whether it will reach the Light River, an important environmental asset; and (2) the residence time of the injectant in the aquifer. This study demonstrates how these questions can be addressed by using a combination of multiple geophysical techniques and stochastic groundwater modeling.

2.2. Hydrogeological data

Kapunda is located within the Adelaide Geosyncline, a major geological province in central South Australia. The local geology is dominated by Neoproterozoic aged formations (Lambert et al., 1980). The main geological formations in the study area include the Tapley Hill Formation to the north, which covers the hypothetical SELT site, and the Brighton Limestone to the south. The Tapley Hill Formation primarily consists of blue-grey laminated siltstone and slate, while the Brighton Limestone is typically characterized by coarse-grained and recrystallized marble units (Akker and Watson, 2017). From a hydrogeological perspective, these formations behave as an interconnected fractured rock aquifer, the hydraulic behavior of which is largely governed by the secondary porosity developed from fracturing (Jeuken and Magarey, 2017).

A total of 42 observations wells were used in this study (Fig. 1), most of which only have a single groundwater level reading, often collected in the 1970s. There are no metered groundwater usage data in Kapunda. As groundwater EC is relatively high in Kapunda, ranging between 1900 and 22,000 $\mu\text{S}/\text{cm}$ with a mean of 5800 $\mu\text{S}/\text{cm}$ (~ 3300 mg/L total dissolved solids), groundwater usage is assumed to be negligible.

Hydraulic conductivity was estimated from well yield and draw-down data using Logan Approximation (Logan, 1964) by Jeuken and Magarey (2017). This approach provided 28 estimates of hydraulic conductivity (Fig. 1) ranging between 0.0007 and 0.4 m/d, with a geometric mean of 0.04 m/d. The error of this method is likely to be in the order of $\pm 50\%$ (Logan, 1964). In addition, a 9-hour aquifer test was performed in February 2020 in the northern part of the study area (Fig. 1) and reported a hydraulic conductivity of 0.07 m/d. Effective porosity was estimated to be 1% near the aquifer test site based on fracture logging using a downhole optical scanner to ~ 65 m depth and assuming 50% cementation (Jeuken and Magarey, 2017).

An initial assessment of groundwater recharge was undertaken using the chloride mass balance method (Wood, 1999). This technique assumes 1D vertical advective flow only and no chloride derived from flow upgradient of the bores. The chloride mass balance equation is as follows:

$$\text{Recharge} = \frac{\text{Rainfall} \times \text{Cl}_{\text{Rainfall}}}{\text{Cl}_{\text{Groundwater}}} \quad (1)$$

where Cl is chloride concentration (mg/L). In Kapunda, the average chloride concentration is ~ 9 mg/L in rainfall (Davies and Crosbie, 2018) and ~ 1100 mg/L in groundwater according to the observation well data. Based on this analysis, the long-term average recharge rate is ~ 4 mm/y, which is $\sim 0.8\%$ of rainfall. Note that this method estimates net recharge, which already accounts for groundwater evapotranspiration.

The regional groundwater sink is the Light River. Lamontagne et al. (2020) applied various environmental tracers, including δD and $\delta^{18}\text{O}$ of water, EC, chloride and radon-222, to evaluate the surface water – groundwater connectivity of the Light River. They estimated baseflow to the Light River within our study area in 2019 to be in the order of 400–3000 m^3/d . They also identified a zone of higher groundwater discharge in the eastern part of our study area (i.e. upstream of A' in Fig. 1).

2.3. Geophysical data

2.3.1. Audio-frequency magnetotellurics

AMT is an electromagnetic method that uses naturally-occurring, passive electromagnetic field sources, such as global lightning strikes, to map geological structures (Garcia and Jones, 2002). Timevarying magnetic fields induce electrical currents into the earth that can be measured using grounded dipoles and magnetic field antennas over a wide range of frequencies (Vozoff, 1991). The

received signal is used to estimate ground electrical resistivity and the depth of investigation is generally in kilometers (Spies, 1989).

As part of this study, a broadband, audio-frequency magnetotellurics (AMT) survey was undertaken in April 2019 on a grid of 87 sites with a nominal spacing of 100 m (Fig. 1). Data were recorded at each site for about 20 h using the Phoenix MTU-5A systems, yielding good quality AMT responses in the bandwidth of 1–10,000 Hz.

The collected AMT data were inverted in 3D using ModEM (Kelbert et al., 2014). The model consists of 100 cells in the east-west direction and 120 cells in the north-south direction with a minimum cell dimension of 12 m. The vertical dimension was discretized into 120 layers with a minimum thickness of 5 m, increasing at a rate of 2% with depth. Impedance error floors were set to 7% for all components. The inversion included 26 frequencies, spread evenly from 0.001 to 100 Hz with five estimates per decade. The model roughness was set with a tau of 0.1 and no weighting was applied for either horizontal or vertical smoothing. The model misfit with the data has a root mean square error (RMSE) of 1.9.

The electrical conductivity (EC) estimates from the 3D inversion at 50 and 100 m depth are shown in Fig. 2. The 50 m depth slice shows two distinctly different zones in the study area. The more conductive zone to the north is interpreted to be related to the Tapley Hill Formation, while the more resistive zone to the south is interpreted to be related to the Brighton Limestone. The 100 m depth slice indicates that EC generally decreases with depth. In addition, phase tensor analysis of the high frequency AMT data suggests that the top 100 m of the fractured rock aquifer is electrically isotropic over the survey area, possibly due to deep-weathering of the existing bedrock fabric.

The EC estimates from the inverted AMT data can also be used to provide information on hydraulic conductivity via the following petrophysical relationship (Purvanec and Andricevic, 2000):

$$EC = aK^b \quad (2)$$

where K is hydraulic conductivity (m/d), and a and b are empirical constants, which were calibrated using data from the aquifer test and the closest AMT station. With a hydraulic conductivity of 0.07 m/d (Section 2.2) and a geometric EC mean of $\sim 520 \mu\text{S}/\text{cm}$, it was estimated that $a = 950$ and $b = 0.23$.

While there are other non-linear petrophysical relationships to relate EC and K (Slater, 2007), a linear log-log relationship (Eq. (2)) was adopted in this study for reasons of parsimony, which has the potential to cause bias in the model predictions. The investigation of different petrophysical relationships on the predictive uncertainty, however, is beyond the scope of this study.

2.3.2. Time-domain electromagnetics

TEM involves applying a direct current to a transmitter loop and then shutting the current off abruptly (Everett, 2013). This produces a timevarying magnetic field into the earth, subsequently generating eddy currents in subsurface conductors. Such eddy currents create a secondary magnetic field that is measured by a receiver loop. The decay rate of the secondary magnetic field is directly related to ground electrical resistivity (Everett, 2013). Compared to AMT, TEM generally has a shallower depth of investigation but a finer resolution at the near-surface (Spies, 1989).

A TEM survey was conducted in May 2019 at 85 sites with a nominal spacing of 100 m. The TEM sites were chosen to be as close to

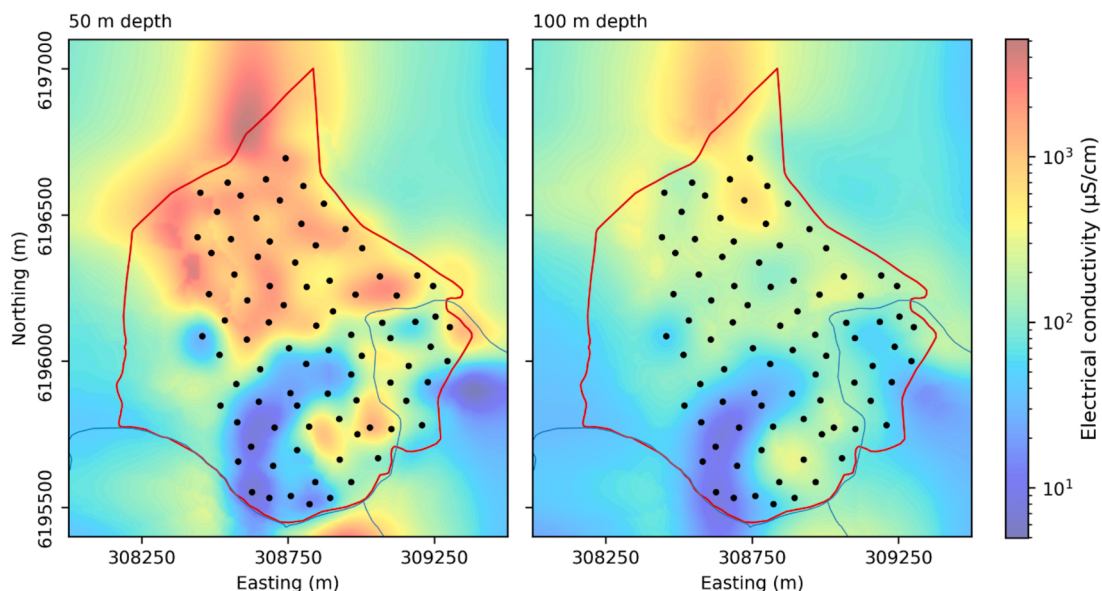


Fig. 2. EC depth slice of the inverted AMT data at 50 and 100 m depth. The black dots denote AMT stations, the red line denotes the study area and the blue lines denote rivers and creeks (For interpretation of the references to colour in this figure legend, the reader is referred to the web version of this article.).

the AMT sites as possible. The soundings were collected using the Zonge Engineering NanoTEM system. This system has fast transmitter turn-off and sampling rate to collect near-surface data down to ~ 80 m depth in our study area. A central loop configuration was used where a single-turn $5 \text{ m} \times 5 \text{ m}$ receiver loop was placed at the center of a single-turn $20 \text{ m} \times 20 \text{ m}$ transmitter loop. The transmitter was set to 2 amps and powered by a 12 V battery. Three data stacks were collected at each station using a repetition rate of 64 Hz and sampling period of $1.6 \mu\text{s}$. The collected TEM data were processed to remove noisy late time data and then inverted in 1D using AarhusInv (Auken et al., 2015) as a smooth 20-layer model.

A transect of the inverted TEM data is shown in Fig. 3. The south-eastern side of the transect (i.e. near A') shows a thin layer with moderate EC near the surface, probably representing the unsaturated zone. It is then followed by a highly conductive layer, possibly indicating the weathered part of the saturated zone with relatively high porosity and groundwater salinity. It then gradually transitions into a more resistive layer, potentially representing the unweathered part of the saturated zone with low porosity. This layering conceptualization is believed to be applicable throughout Kapunda, although the unweathered layer may extend to greater depths in other parts of the area (Figs. 2 and 3).

Given the relative shallowness and high salinity of groundwater in the survey area, the water table is expected to be detectable in the TEM data as an EC high. Therefore, the EC peak of the TEM soundings was used as an indicator of water table depth. Due to a paucity of groundwater level observations for ground-truthing, a quality assurance process was performed on the water table estimates using a pseudo-Bayesian approach, where our prior knowledge is based on a potentiometric surface developed using groundwater level observations and water levels of the Light River. Given the absence of groundwater-affecting activities (e.g. pumping) in the survey area, the potentiometric surface is assumed to be a reasonable approximation of the system. Therefore, only the groundwater levels derived from TEM that are within ± 2 m of our prior knowledge, totaling 23 estimates (Fig. 1), were used in the groundwater model inversion.

2.3.3. Nuclear magnetic resonance

NMR, also known as Magnetic Resonance Sounding (MRS), is a geophysical technique that exploits the quantum physical properties of hydrogen protons in subsurface water to gain hydrogeological information (Legchenko et al., 2002). The initial amplitude of the received signal is directly related to water content, which is a proxy for porosity in the saturated zone. In addition, a decay time constant T_2 is estimated from the decay pattern of the received signal, which provides information about pore size distribution (Behroozmand et al., 2015).

Borehole NMR data were collected in the northern part of the study area (Fig. 1) using Vista Clara's Javelin system equipped with a JPY 350 probe (88.9 mm in diameter) to ~ 28 m depth. The Carr-Purcell-Meiboom-Gill (CPMG) pulse sequence was used (Carr and Purcell, 1954; Meiboom and Gill, 1958). The collected NMR data were processed and inverted using Vista Clara's Javelin Pro Plus program.

The decay time constant T_2 and total water content from the NMR inversion below the water table are shown in Fig. 4. Note that the total water content includes both connected and isolated pores, and it is the former that contributes to groundwater flow. Therefore, the total water content was separated into water content in small, moderate and large pores using T_2 cut-off times of 3 and 33 ms (Behroozmand et al., 2015). We assume groundwater flows primarily in larger pores, hence the water content in large pores was used as a proxy for effective porosity. However, the water content in large pores below ~ 17 m depth appears to be affected by some localized fractures, the porosity of which may not be regionally representative (Fig. 4) and hence was excluded from the analysis. The remaining data indicate a mean effective porosity of 5.6 %. This is considerably higher than the value of 1% as suggested by optical scanning, but is consistent with Akker and Watson (2017) who reported an effective porosity of 5% for the same Tapley Hill Formation, but approximately 80 km south of the study area. The uncertainty in effective porosity is explored further in the groundwater model inversion.

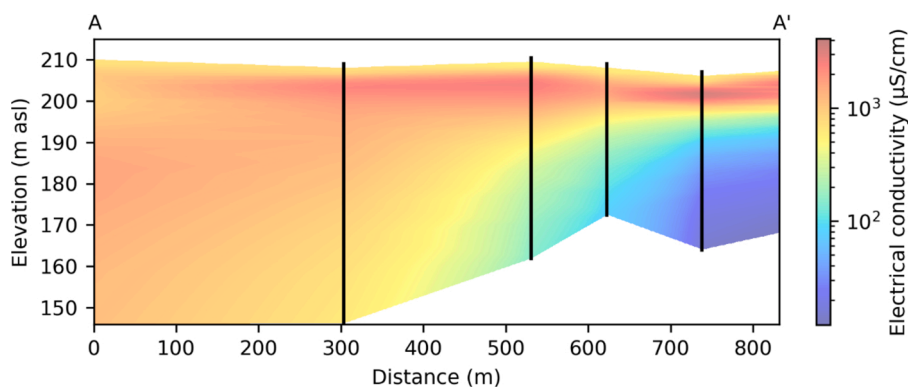


Fig. 3. A transect of the inverted TEM data. The transect location is shown in Fig. 1. The black lines denote TEM stations; asl stands for above sea level.

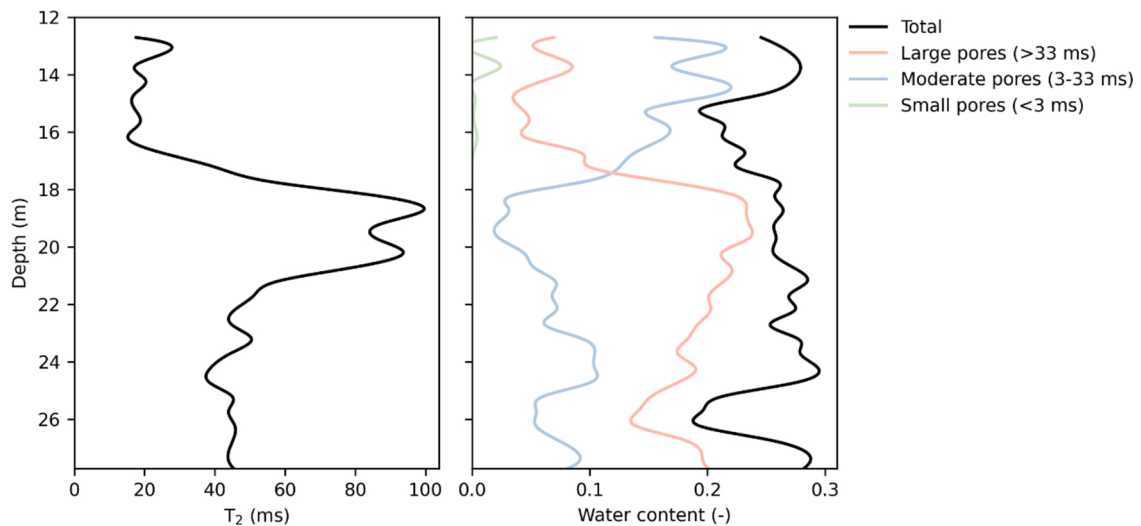


Fig. 4. Profiles of the decay time constant T_2 (left) and water content (right) from the NMR inversion. The water content in large pores is assumed to be a proxy for effective porosity.

2.4. Groundwater modeling

2.4.1. Model development

Due to the lack of detailed fracture data at a regional scale in Kapunda, the fractured rock aquifer was simulated using the equivalent porous medium approach (Long et al., 1982). Also, despite the importance of rapid flow paths in contaminant transport problems, a dual porosity scheme was considered beyond the scope of this study and should be acknowledged as a model limitation.

A 3D regional-scale numerical groundwater model was developed using MODFLOWUnstructured Grid (USG) (Panday et al., 2017). The model domain is $5.5 \text{ km} \times 5.2 \text{ km}$ in area and the model edges were set $\sim 2 \text{ km}$ away from the study area to avoid boundary effects (Fig. 1). The Voronoi grid was generated using AlgoMesh (Merrick, 2016) with a nominal cell size of 10 m^2 in the study area and up to $\sim 25,000 \text{ m}^2$ in the regional area. The same grid was applied to two layers, resulting in a total of 294,356 cells.

The top layer of the model represents the more permeable, weathered part of the fractured rock aquifer, while the bottom layer represents the less permeable, unweathered part of the aquifer. The top model surface was sourced from the DEM that has a resolution of $5 \text{ m} \times 5 \text{ m}$. The thickness of the weathered layer was estimated using the AMT data, where the EC sounding at each station was divided into two layers using the K-means clustering technique (Jain, 2010), assuming electrical and hydraulic properties are related. These thickness estimates were interpolated within the AMT survey area and extrapolated to their geometric mean of $\sim 100 \text{ m}$ outside the survey area. A constant thickness of 100 m was applied to the bottom layer, allowing all observation wells to be included in the model.

The Light River and other ephemeral creeks were simulated using MODFLOW's RIV package (Panday et al., 2017). Time-varying river depths were used for the Light River based on data from the nearest gauging station. The local ephemeral creeks are usually dry except for the wetter winter months, hence their river depth was set to 0 m (i.e. river stage equals riverbed elevation). River bathymetry was sourced from the DEM. Riverbed conductance was mostly set to $0.1 \text{ m}^2/\text{d}$ based on the regional hydraulic conductivity (Section 2.2), except for the eastern part of the Light River in the study area where a higher conductance of $10 \text{ m}^2/\text{d}$ was applied, as this reach was identified to be a zone of higher groundwater discharge (Lamontagne et al., 2020). The historical mine and quarry were represented as groundwater discharge features using MODFLOW's DRN package (Panday et al., 2017). The drain elevation was sourced from the DEM and the drain conductance was set to $0.1 \text{ m}^2/\text{d}$. The regional lateral groundwater inflows from the northern and southern sides were modeled in both layers using MODFLOW's GHB package (Panday et al., 2017). The head values were derived from groundwater level observations and the conductance was set to $0.1 \text{ m}^2/\text{d}$.

Net groundwater recharge was simulated using MODFLOW's RCH package (Panday et al., 2017). Annually-varying rainfall data were incorporated into the model as recharge multipliers, which were multiplied with the spatially-varying rainfall-to-recharge ratios (a calibration parameter) to derive net recharge. Groundwater evapotranspiration is not explicitly included in the model as it is already accounted for in net recharge. Given the relatively high groundwater salinity in Kapunda (Section 2.2), groundwater extraction is assumed to be negligible and hence not simulated in the model.

The model consists of 53 stress periods. The first period is steady-state and represents the pre-1970 period, which was selected based on the observation data availability. This stress period provides the initial conditions for the subsequent 50 transient annual stress periods, which represent the time period between 1970 and 2019 and were used for history-matching. The last two stress periods represent the hypothetical SELT operation and remediation phase, with a duration of two months and three years respectively. All transient stress periods have 10 time steps and a time step multiplier of 1.2.

The hypothetical SELT operation consists of four injection wells, separated by 20 m , and one extraction well at the center. The

operation rate is 0.02 L/s for each injection well and 0.1 L/s for the extraction well. During the remediation phase, the extraction well continues to operate at the same rate of 0.1 L/s while all the injection wells are switched off.

Transport of the injectant was simulated using the particle-tracking code mod-PATH3DU (Craig et al., 2020). The only transport mechanism modeled is advection, while processes such as dispersion, chemical reaction and sorption are considered beyond the scope of this study. A circle of 12 particles, representing the injectant, were placed around each injection well and released at the commencement of the SELT operation. The model was set to extend the tracking time beyond the end of simulation time by using the flow field from the last time step.

2.4.2. Model inversion

Groundwater model inversion was performed using the ensemble-smoother method via PESTPPIES (White, 2018). A brief description of the ensemble-smoother method is provided here and readers are referred to White (2018) and Chen and Oliver (2013) for further details. The ensemblesmoother method reformulates the GLM algorithm by empirically deriving the Jacobian matrix from an ensemble of random parameter values (Chen and Oliver, 2013):

$$\Delta_{\theta} = - \left(\left(J_{emp}^T \Sigma_{\epsilon}^{-1} J_{emp} \right) + (1 + \lambda) \Sigma_{\theta}^{-1} \right)^{-1} \left(\Sigma_{\theta}^{-1} (\Theta - \Theta_0) + J_{emp}^T (D_{sim} - D_{obs}) \right) \tag{3}$$

where

$$J_{emp} \approx \Sigma_{\epsilon}^{\frac{1}{2}} \Delta_{sim} \Delta_{par}^{-1} \Sigma_{\theta}^{-\frac{1}{2}} \tag{4}$$

$$\Delta_{sim} = \frac{\Sigma_{\epsilon}^{-\frac{1}{2}} (D_{sim} \ominus \bar{D}_{sim})}{\sqrt{N_c - 1}} \tag{5}$$

$$\Delta_{par} = \frac{\Sigma_{\theta}^{-\frac{1}{2}} (\Theta \ominus \bar{\Theta})}{\sqrt{N_c - 1}} \tag{6}$$

where Δ_{θ} is the parameter upgrade matrix, J_{emp} is the empirically-derived Jacobian matrix, Σ_{ϵ} is the observation noise covariance

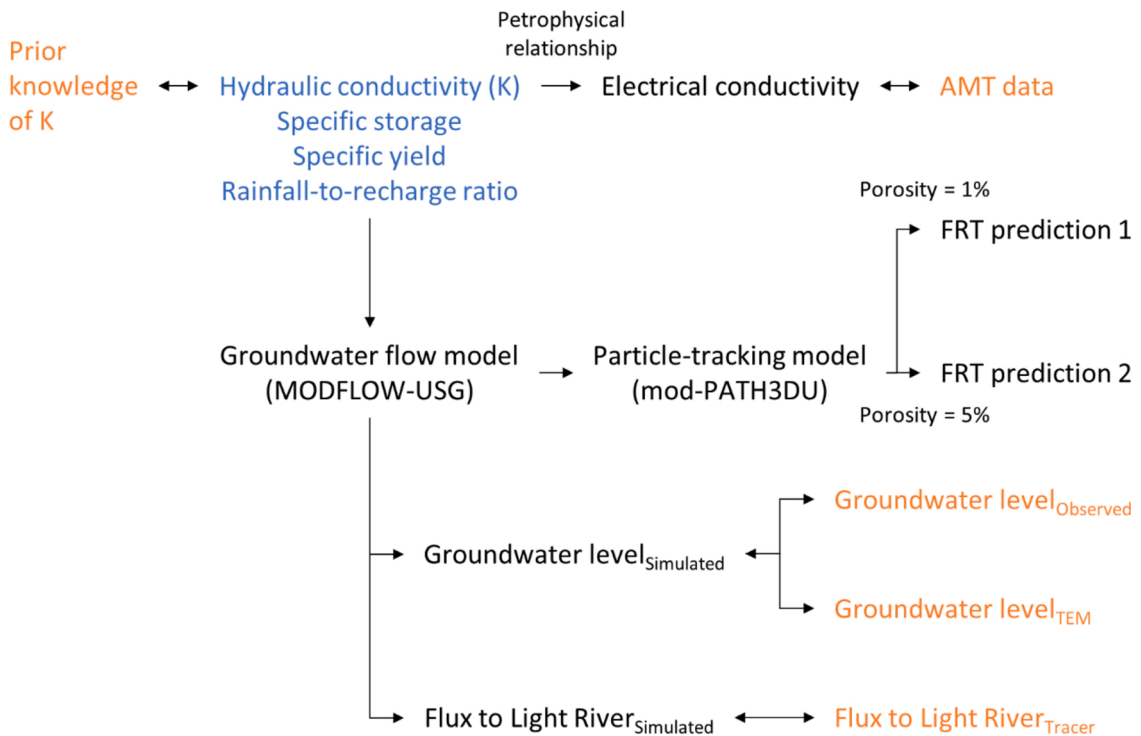


Fig. 5. Inversion workflow in this study: parameter groups that were varied during the inversion are in blue color, observation groups that were used as inversion targets to compute the objective function are in orange color. Due to the uncertainty in effective porosity and the lack of inversion targets, two separate particle-tracking runs were undertaken with different uniform effective porosity values of 1% and 5%. Each double arrow denotes a residual calculation (For interpretation of the references to colour in this figure legend, the reader is referred to the web version of this article.).

matrix, Σ_{θ} is the prior parameter covariance matrix, λ is the Marquardt dampening parameter, Θ and Θ_0 are the current and initial parameter vector respectively, D_{obs} and D_{sim} are the observation and simulated-equivalent ensembles respectively, \bar{D}_{sim} and $\bar{\Theta}$ are the mean of the simulated-equivalents to observations and parameters across their respective ensembles respectively, N_e is the number of realizations, and \ominus denotes broadcast subtraction.

In this study, the ensemble size was initially set to 105 realizations to account for situations where some realizations may fail to converge. The dampening of the parameter upgrade factor is controlled by λ (Eq. (3)), where a high value of λ leads to rapid improvement in the objective function, while a low value of λ is better at navigating the objective function space. The optimal value for λ is automatically estimated for each inversion iteration through a trial-and-error procedure based on a subset of the parameter ensemble (the whole ensemble is not used to reduce computational time). In this study, the inversion was converged after 9 iterations based on the following termination criteria: (1) if the relative decrease in the mean objective function was less than 1% over 3 iterations, or (2) if there was no reduction in the mean objective function for 3 iterations. The top 100 realizations with the smallest objective function were used to form the final ensemble.

The inversion workflow in this study is illustrated in Fig. 5. The modeled hydraulic conductivity was compared with our prior knowledge, including the aquifer test and Logan Approximation estimates. In addition, to provide more constraints in the study area, the modeled hydraulic conductivity was compared with the AMT data. This was achieved by converting the hydraulic conductivity field to an EC field using Eq. (2) and the empirical constants estimated in Section 2.3.1. The empirical constants are assumed to be spatially uniform due to the limited aquifer test data. Given the uncertainty in the petrophysical relationship, the AMT data were aggregated into five zones using the K-means clustering technique (Jain, 2010). The EC comparison was only undertaken for the weathered layer as the unweathered layer possesses a different electrical property (Figs. 2 and 3) where the estimated empirical constants may not apply.

Groundwater levels computed by the flow model were compared with groundwater levels from the observation wells and TEM. In addition, the simulated groundwater flux to the Light River within the study area in 2019 was compared with the mean of tracer estimates from Lamontagne et al. (2020).

It is worth noting that effective porosity was not included as a calibration parameter. While the ensemble smoother method allows the inclusion of all parameters in the history matching procedure as long as there is a covariance matrix to constrain parameter values, the prior and posterior probability distribution of effective porosity are expected to be similar due to the lack of inversion targets for particle tracking. Therefore, the inclusion of effective porosity in the history matching procedure is believed to have minimal contribution to the prediction uncertainty quantification. As such, given the model objective, the uncertainty associated with effective porosity was assessed by undertaking two separate particle-tracking runs with different uniform effective porosity values of 1% and 5%, which are considered to represent the lower and upper bounds respectively.

Pilot points, a method for spatial parameterization, were used for all parameter groups (Doherty, 2003). Given the fractured rock environment, pilot points were placed at each observation to capture the local heterogeneity. In addition, gaps in the pilot point coverage were filled using a maximum separation distance of 25 m in the study area and 250 m elsewhere in the weathered layer, and 500 m in the unweathered layer. This resulted in 1397 pilot points in the weathered layer and 103 pilot points in the unweathered layer for each corresponding parameter group. Spatial correlation between the pilot points were defined using an exponential variogram, with nugget = 0, sill = 1 and $a = 1100$, where “a” describes the decay rate of spatial correlation with distance and was set to $\sim 20\%$ of the model extent.

The calibration parameters are detailed in Table 1. All parameters were log-transformed during the inversion. The prior parameter variance was calculated based on the assumption that the difference between the upper and lower bound of a parameter group is equal to four standard deviations of its prior probability distribution (White, 2018). Based on the AMT data, horizontal hydraulic conductivity is assumed to be isotropic (i.e. $K_x = K_y$). A similar assumption was adopted for vertical hydraulic conductivity (i.e. $K_{\text{horizontal}} = K_{\text{vertical}}$). The effect of this assumption is expected to be small given the relatively low permeability of the unweathered layer and therefore the already dominant lateral flow. Hydraulic conductivity of the unweathered layer was forced to be at least an order of magnitude lower than the hydraulic conductivity of the weathered layer. It is worth noting that while the potentially connected high hydraulic conductivity pathways are not explicitly represented in the prior, these pathways are expected to be reflected in the AMT data that were included in the history matching procedure (Fig. 5). The storage parameter settings are based on the aquifer tests in the adjacent Barossa region (~ 30 km away) that has a similar hydrogeological setting (Li and Cranswick, 2016). Specific storage was

Table 1

Inversion settings for the parameter groups. The initial and bound parameter values are before log-transformation. Prior parameter variance was calculated based on the assumption that the difference between the upper and lower bound of a parameter group is equal to four standard deviations of its prior probability distribution.

Parameter group	Layer	Initial value	Lower bound	Upper bound	Variance [†]	Source
Hydraulic conductivity (m/d)	1	0.1	$1e^{-5}$	1	1.562	Aquifer test Logan Approximation
Hydraulic conductivity (m/d)	2	$1e^{-4}$	$1e^{-5}$	$1e^{-3}$	0.25	Aquifer test Logan Approximation
Specific storage (m^{-1})	2	$1e^{-6}$	$1e^{-7}$	$1e^{-5}$	0.25	Li and Cranswick (2016)
Specific yield (-)	1	0.01	0.001	0.05	0.18	Li and Cranswick (2016)
Rainfall-to-recharge ratio (-)	1	0.008	$1e^{-4}$	0.05	0.455	Chloride mass balance

[†] Based on log-transformed parameter values.

predominately used for the bottom layer, which is confined, and for simplicity the same values were applied to the top layer (vice versa for specific yield). The rainfall-to-recharge ratios vary spatially but were fixed with time for parsimony reasons.

The observation groups are detailed in Table 2. Prior observation variance was calculated in a similar fashion to the prior parameter variance. The error bounds are assumed to be ± 0.2 m for groundwater levels from the observation wells (Rau et al., 2019), ± 2 m for groundwater levels derived from TEM and ± 50 % for prior knowledge of hydraulic conductivity (Logan, 1964). The bounds for the EC and baseflow observation groups are based on the actual range of the AMT data and tracer estimates (Lamontagne et al., 2020). The EC, hydraulic conductivity and baseflow observations were log-transformed. The prior observation variance values were used to derive the random observation ensemble and observation weights, the latter were then adjusted using the program PWTADJ1 (Doherty et al., 1994), which automatically scales the observation weights so that all observation groups are equally visible in the objective function.

3. Results

3.1. History-matching performance

The history-matching performance of the model ensemble for all observation groups is shown in Fig. 6. For groundwater levels from the observation wells, the residual map shows some potential conflicts between data, where positive residuals are adjacent negative residuals. This may be caused by local heterogeneity given the fractured rock environment, or simply a measurement error, which cannot be resolved with the currently available data. The scatter plot shows a reasonable match between the observed and simulated values, with the cloud of points being centered around the 1:1 line and a scaled root mean square error (SRMSE, calculated as RMSE divided by the observation range) of 7.3 %.

For groundwater levels derived from TEM, both the residual map and scatter plot show an overall overestimation by the model. This potentially suggests that the peak of EC profile may be a sub-optimal indicator of true water table depth. It is possible that the top of the saturated zone may have been diluted by mixing with the relatively fresh rainwater, or there is a significant capillary zone. Nevertheless, an RMSE of 1.3 m is considered to be within the uncertainty bounds of these groundwater level estimates.

Prior knowledge of hydraulic conductivity includes the aquifer test data and Logan Approximation estimates. The prior knowledge functions like regularization in that the objective function is penalized as the modeled values deviate from the prior values. It is worth noting that hydraulic conductivity is a model input, not an output that requires calculation like groundwater levels, and hence is relatively easy to fit. The misfit of hydraulic conductivity between the prior and modeled values is a trade-off for the inversion to fit other observation groups, especially groundwater levels from the observation wells as most of the prior hydraulic conductivity values are located outside the study area. The misfit suggests a potential conflict between these two observation groups, which may be caused by the heterogeneous nature of the fractured rock aquifer and/or errors in the Logan Approximation estimates and groundwater level observations.

For the EC observation group, the residual map shows two distinct zones: an underestimated zone to the north and an overestimated zone to the south, which coincide with the location of Tapley Hill Formation and Brighton Limestone respectively. This suggests that using the same petrophysical relationship empirical constants for these two formations is sub-optimal. The fit may be improved by undertaking an additional aquifer test so that a separate set of empirical constants can be derived for each of these formations. The additional aquifer test may also contribute to the improvement of model predictive accuracy.

The simulated baseflow to the Light River within the study area in 2019 ranges between 290 and 780 m^3/d with a mean of 560 m^3/d , which is mostly within the tracer estimate range of 400–3000 m^3/d (Lamontagne et al., 2020), albeit on the lower end of the range. This discrepancy may be due to the difference in time scale between the tracer and modeled estimates and/or the riverbed conductance term used.

3.2. Posterior parameter distribution and uncertainty

The maximum likelihood and logarithmic standard deviation of the posterior distribution for the calibration parameters are shown in Fig. 7. Hydraulic conductivity in the weathered layer is higher in the north-eastern part and lower in the south-western part of the study area. Regionally, there is a substantial permeable zone to the east and a less permeable zone to the west of the study area, potentially indicating the differences in the amount of weathering. The unweathered layer typically has a lower hydraulic

Table 2

Inversion settings for the observation groups. Prior observation variance was estimated by assuming the difference between the upper and lower bound of an observation is equal to four standard deviations of its prior probability distribution.

Observation group	Unit	Number of observations	Variance
Groundwater levels from observation wells	m asl	42	0.01
Groundwater levels from TEM	m asl	23	1
Zoned EC from AMT †	$\mu\text{S}/\text{cm}$	5	0.008 – 0.03
Prior knowledge of hydraulic conductivity †	m/d	29	0.014
Baseflow to Light River †	m^3/d	1	4.57

† Log-transformed.

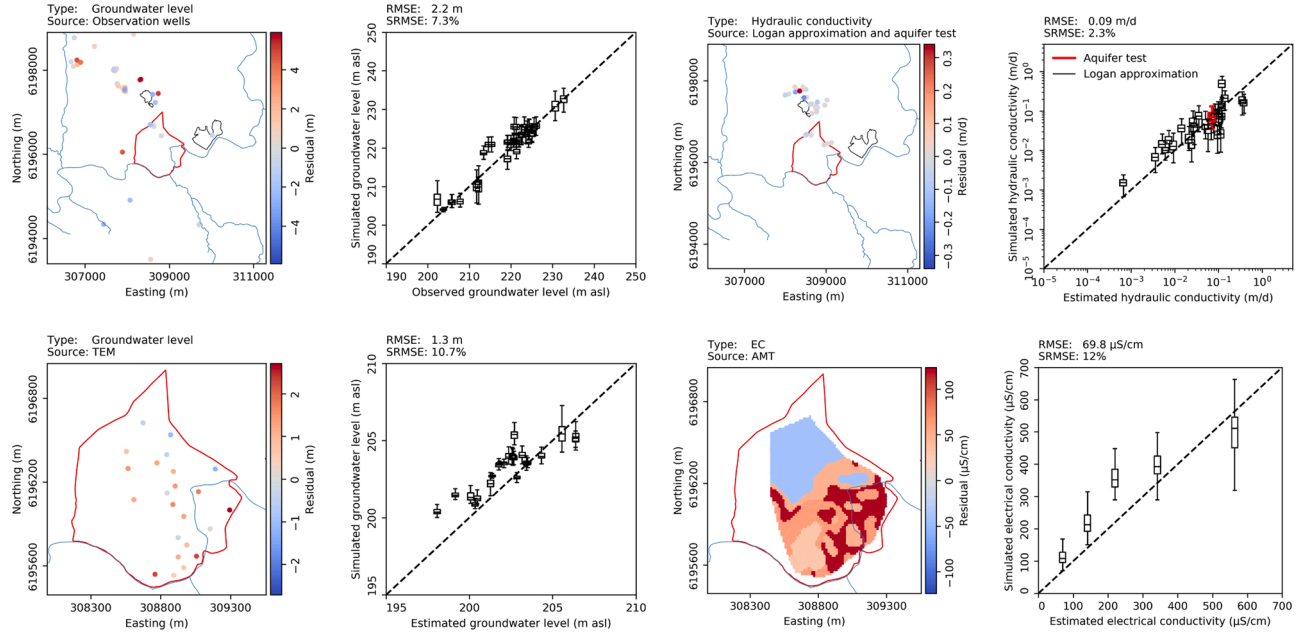


Fig. 6. History-matching performance of the model ensemble for all observation groups. The left column shows the residual maps, where positive value indicates overestimation and negative value indicates underestimation by the model. The right column shows the scatter plots of simulated against target values. The RMSE and SRMSE were calculated based on the maximum likelihood of the simulated values.

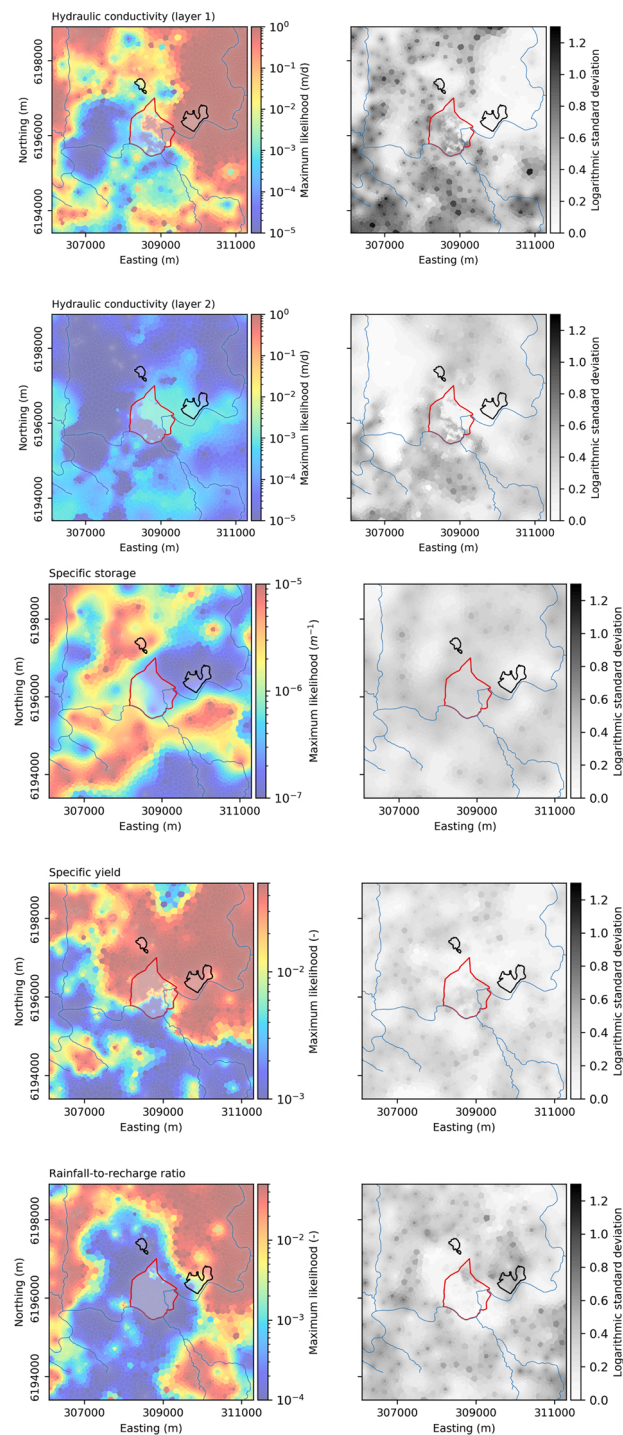


Fig. 7. The maximum likelihood and logarithmic standard deviation of the posterior distribution for the calibration parameters. The logarithmic standard deviation can be used as an indicator of posterior parameter uncertainty.

conductivity, although there is a relatively permeable zone in the north-eastern part of the study area. Specific storage is generally high except to the east and south-east of the study area, while specific yield is higher to the north and lower to the south. The rainfall-to-recharge ratio generally follows topography and is higher in the outer, elevated areas and lower in the center, low-lying areas.

The logarithmic standard deviation in Fig. 7 was calculated using parameter values from the 100 model realizations on a cell-by-cell basis and can be used as an indicator of posterior parameter uncertainty, which is highest for hydraulic conductivity in the weathered layer. Its uncertainty is relatively high in the study area, probably due to the limited physical measurements of groundwater

level in this area. In contrast, the uncertainty is relatively low near the historical mine, which is probably due to the abundance of Logan Approximation estimates in this area (Fig. 1). Both hydraulic conductivity in the unweathered layer and specific yield show a relatively high uncertainty in the southern part of the study area, while the uncertainty of specific storage is relatively uniform. Although the uncertainty of rainfall-to-recharge ratio is considerably high in the regional areas, it is relatively low in most part of the study area.

3.3. Prediction distribution and uncertainty

The predicted injectant flow paths for the hypothetical SELT operation are shown in Fig. 8. For an effective porosity of 1%, 95 out of the 100 model realizations indicate that all of the injectant may be retrieved, while 5 realizations show that the injectant has the potential to reach the Light River. For an effective porosity of 5%, 99 out of the 100 model realizations suggest complete removal of the injectant and only 1 realization shows the potential for injectant to reach the river. As the travel speed of injectant is inversely proportional to effective porosity, the injectant travels at a slower speed in the 5% porosity scenario and hence has a higher probability to be completely retrieved. The modeling suggests that it would take 9–175 years after the SELT commencement for the injectant to reach the river, with a median of ~35 years. It is important to note that these model runs represent the worst-case scenario as processes such as degradation and attenuation are not considered in the modeling.

It is worth noting that the injectant under consideration is highly biodegradable. It is expected that ~90 % of the injectant will degrade completely within 28 days of exposure to groundwater (ECHA, 1999; Hidalgo et al., 2019, 2020). Our modeling shows no

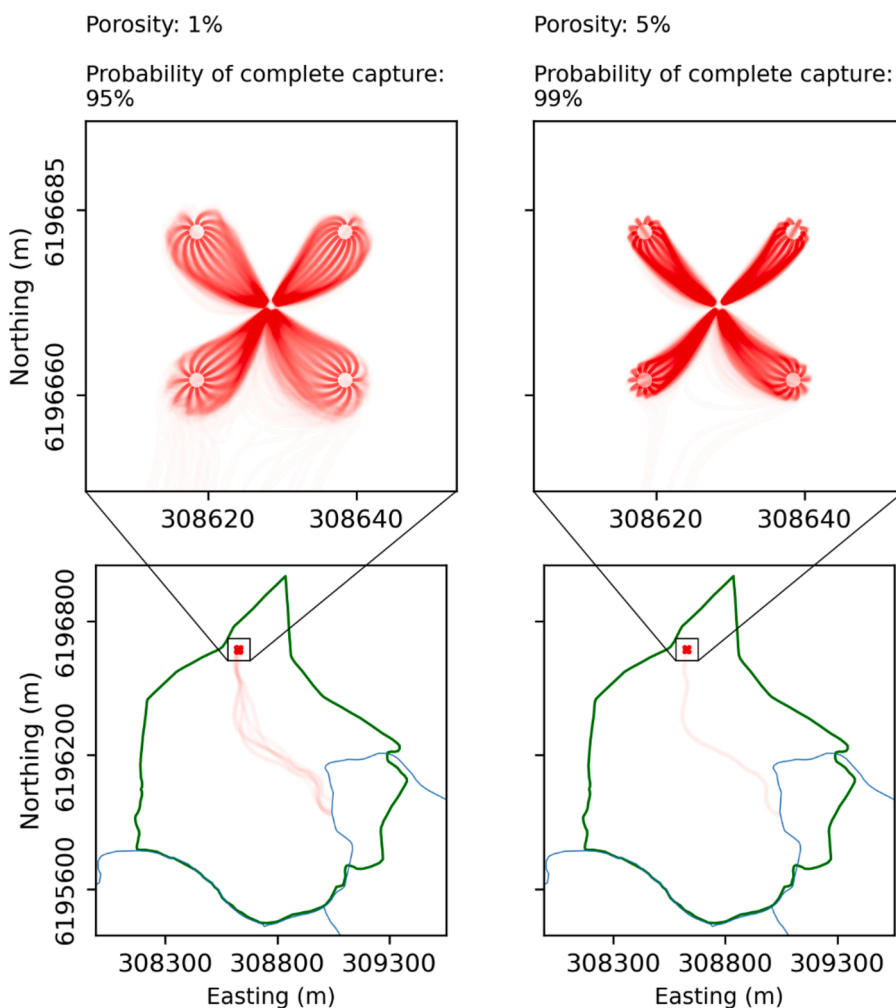


Fig. 8. Predicted injectant flow paths for the hypothetical SELT operation and the probability of completely capturing the injectant for different effective porosity values of 1% and 5%. Note that the injectant under consideration is highly biodegradable (~90 % degradation over 28 days). Our modeling shows no evidence that the injectant can leave the SELT site or reach the Light River within this timeframe. The red lines denote injectant flow paths, the opacity of the red lines denotes likelihood, the green line denotes the study area and the blue line denotes rivers and creeks (For interpretation of the references to colour in this figure legend, the reader is referred to the web version of this article.).

evidence that the injectant can leave the SELT site, much less reach the Light River within this timeframe.

Further analysis was performed on the injectant residence time in the aquifer after the SELT commencement (Fig. 9). This analysis assumes that the injectant does not degrade with time. For an effective porosity of 1%, the results suggest that most of the injectant may be retrieved between 200 and 400 days after the SELT commencement. This relatively long residence time was unexpected given the small scale of the SELT operation and is likely due to the need of some injectant to travel against the regional groundwater flow gradient to reach the extraction well. The relatively low extraction rate and permeability (compared to sedimentary aquifers) may also contribute to this relatively long residence time. For an effective porosity of 5%, the results indicate that there may still be up to 20 % of injectant remaining in the aquifer even after 1000 days, potentially suggesting a longer remediation phase and/or a higher extraction rate may be needed. Again, it is important to note that these residence time results represent the worst-case scenario and do not consider the biodegradability of the injectant.

4. Discussion

There are various levels of coupling geophysics and groundwater modeling, ranging from basic manual conceptual interpretation (e.g. Harrington et al., 2014) to sequential inversion (e.g. Christensen et al., 2017) to joint inversion (e.g. Herckenrath et al., 2013). For sequential inversion, outputs from geophysical inversion are used for groundwater model inversion, while for joint inversion both the geophysical and groundwater models are inverted simultaneously. This study performed a relatively complex sequential inversion that uses AMT, TEM and NMR data to constrain stochastic groundwater modeling. This method facilitates the flow of information from geophysical and hydrogeological data to the groundwater model prediction of interest.

The challenge of coupling geophysics with groundwater modeling is that geophysical techniques rarely provide direct information about hydrogeological properties. Additional methods and assumptions, such as petrophysical relationships, are often required to bridge this gap, potentially increasing the uncertainty of geophysically-derived observations, as these relationships may vary depending on local site conditions. When using these observations as targets in groundwater model inversion, it is critical to quantify and account for their uncertainty to avoid incorrectly biasing model outcomes. The ensemble-smoother method potentially provides a means to achieve this via the prior observation variance (Table 2), which expresses observation uncertainty as a prior probability distribution. For a given observation, a random sample is drawn from its prior probability distribution for each realisation, forming an ensemble of random observations. This allows the inversion to fit to the observation distribution, which incorporates the observation uncertainty, instead of the observation itself, which may be uncertain especially for the geophysically-derived observations.

There are some limitations in the modeling presented in this paper. Firstly, it is worth noting that the ensemble-smoother method may not necessarily converge to the global minimum of the objective function space, unlike other stochastic methods such as Markov-Chain Monte Carlo. By using the ensemble-smoother method, a compromise is implicitly made where some accuracy in the posterior parameters and predictions is sacrificed for computational efficiency. Secondly, as with most other Bayesian-based techniques, the ensemble-smoother method is dependent on the priors, the derivation of which may sometimes be subjective for geophysically-derived observations. In this study, the TEM data were used to estimate groundwater levels in the study area, which are acknowledged to be uncertain. We assumed the error to be ± 2 m and expressed this uncertainty as a prior observation variance (Table 2), which was then

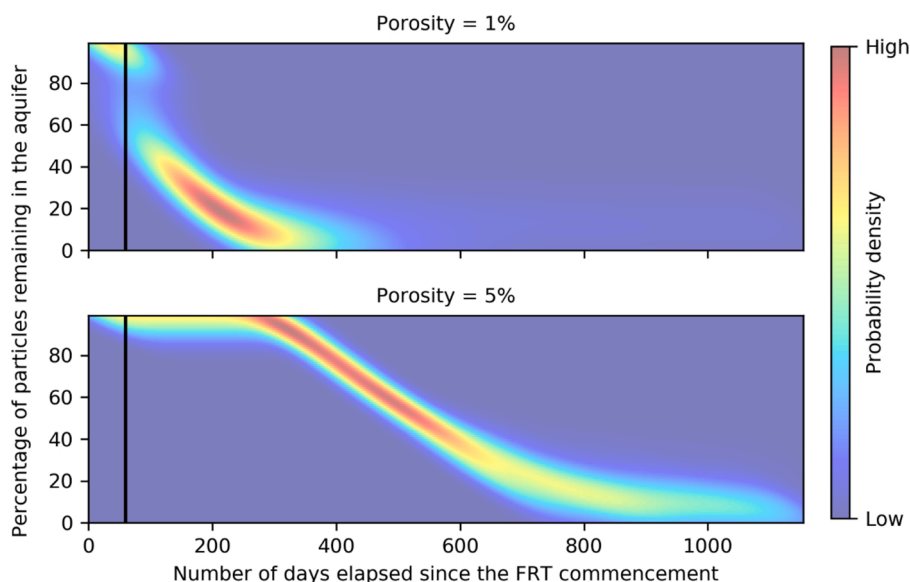


Fig. 9. Predicted injectant residence time in the aquifer since the SELT commencement for different effective porosity values of 1% and 5%. Note that these residence time results represent the worst-case scenario and do not consider the biodegradability of the injectant (~ 90 % degradation over 28 days). The vertical black line denotes when the SELT ceases.

incorporated into the groundwater model inversion. This error bound is a subjective estimation based on our hydrogeological knowledge of the area. Nevertheless, we demonstrated how multiple geophysical techniques can be used to provide a large set of soft data to aid groundwater model development, especially in areas with limited drillhole information, and more importantly, how the uncertainty in these soft data can be expressed in a transparent and repeatable framework that can be reviewed and adjusted as needed.

As for site-specific limitations, there are some areas in the model where the parameters are at their upper bound, especially hydraulic conductivity in the weathered layer and recharge (Fig. 7). It is hypothesised that the baseflow estimate may be too high, forcing these parameters to reach their upper bound. This hypothesis can be tested by collecting more field data, including baseflow analysis and aquifer tests. Meanwhile, the EC estimates from the AMT inversion were used to provide information on hydraulic conductivity via a petrophysical relationship. This requires calibrating the empirical constants against field data, ideally aquifer test data. Due to the limited aquifer test data in the study area, we assumed the empirical constants to be spatially uniform. The model results suggest that this approach may be sub-optimal when applied across multiple geological formations with variable electrical properties. The model results are likely to be improved if an additional aquifer test was performed so that a separate set of empirical constants could be derived for each of these formations.

It is worth noting the difference between the predictive scale and data scales. Spatially the former is mostly between the SELT site and the Light River (i.e. within the study area). In comparison, most of the hydrogeological data, including groundwater level observations and hydraulic conductivity estimates, lie outside the study area (Fig. 1). Therefore, the model predictions are likely to be influenced more by the geophysically-derived groundwater levels and hydraulic conductivity estimates (i.e. NanoTEM and AMT data) within the study area. There is considerable uncertainty associated with these geophysically-derived datasets and it is therefore important to incorporate their uncertainty explicitly in the modelling workflow as demonstrated in this study.

Transport predictions are preferentially sensitive to rapid transport pathways such as along fractures rather than the average media properties provided from an aquifer test. The direct use of aquifer test data for improving model predictive accuracy may therefore be limited. Instead, as demonstrated in this study, aquifer test data can be used to provide constraints for the petrophysical relationship that relates K and EC , which is critical as the EC distribution contains information about the rapid transport pathways.

5. Conclusions

In this study, we coupled multiple geophysical techniques with stochastic groundwater modeling to predict the regional-scale hydrological impact of a hypothetical ISR trial operation for copper recovery in Kapunda, South Australia. The geophysical techniques, including AMT, TEM and NMR, were used to provide constraints on hydraulic conductivity, water table depth, hydrostratigraphy and porosity in a data sparse region. The groundwater model was used as a data assimilation tool to facilitate the flow of information from the geophysical and hydrogeological data to the model prediction of interest. This was achieved using the ensemble-smoother method via PESTPP-IES, which produced an ensemble of 100 calibrated models with a reasonable history-matching performance (an average SRMSE of 7.3 % for groundwater level observations). These calibrated models can be considered to represent the posterior distribution of parameters and predictions that can be readily used for non-linear uncertainty analysis and probabilistic predictions. The model ensemble shows no evidence that the injectant can leave the SELT site or reach the Light River within its biodegradation timeframe.

The challenge of coupling geophysics with groundwater modeling is that geophysical techniques rarely provide direct quantification of hydrogeological properties. Additional methods, such as petrophysical relationships, are required to bridge this gap, potentially increasing the uncertainty of geophysically-derived observations. When using these observations as targets in groundwater model inversion, it is critical to quantify and account for their uncertainty to avoid incorrectly biasing outcomes. The ensemble-smoother method potentially provides a means to achieve this via the prior observation variance and random observation ensemble, allowing the inversion to fit to the observation distribution, which incorporates the observation uncertainty, instead of the observation itself. However, as with most other Bayesian-based techniques, the ensemble-smoother method is dependent on the priors, the derivation of which may sometimes be subjective for geophysically-derived observations. Nevertheless, we demonstrated how multiple geophysical techniques can be used to provide a large set of soft data to aid groundwater model development, especially in areas with limited drillholes, and more importantly, how the uncertainty in these soft data can be expressed in a transparent and repeatable framework that can be reviewed and adjusted as needed.

Author statement

Chris Li

- Conceptualization
- Methodology
- Validation
- Formal analysis
- Data Curation
- Writing – Original Draft
- Writing – Review & Editing
- Visualization

Rebecca Doble

- Conceptualization
- Methodology
- Validation
- Resources
- Writing – Review & Editing
- Supervision
- Project administration

Michael Hatch

- Conceptualization
- Methodology
- Validation
- Formal analysis
- Investigation
- Resources
- Writing – Review & Editing
- Supervision

Graham Heinson

- Conceptualization
- Methodology
- Validation
- Resources
- Writing – Review & Editing
- Supervision
- Project administration
- Fund acquisition

Ben Kay

- Formal analysis
- Investigation

Declaration of Competing Interest

The authors report no declarations of interest.

Acknowledgements

This research is supported by an Australian Government Research Training Program Scholarship and a CSIRO Research Plus Scholarship. We would like to thank Jeremy White, Matthew Knowling, Luk Peeters, Andrew Taylor, Chris Turnadge and Elliot Grunewald for their technical advice and assistance; Leon Faulkner, Philippa Faulkner, Ben Jeuken and Sébastien Lamontagne for providing site data and information. Geophysical and hydrological data are provided from a CRC-P program entitled “Kapunda In-Situ Copper and Gold Field Recovery Trial”. We thank the landholders and the Light Regional Council for access to undertake measurements. AuScope, Geoscience Australia and CSIRO are thanked for providing access to field equipment.

Appendix A. Supplementary data

Supplementary material related to this article can be found, in the online version, at doi:<https://doi.org/10.1016/j.ejrh.2021.100841>.

References

Akker, J.V.d., Watson, T., 2017. Bird-in-Hand Gold Project Groundwater Assessment. AGT report 1300-14-TAB, Adelaide.

- Auken, E., et al., 2015. An overview of a highly versatile forward and stable inverse algorithm for airborne, ground-based and borehole electromagnetic and electric data. *Explor. Geophys.* 46 (3), 223–235. <https://doi.org/10.1071/eg13097>.
- Behroozmand, A.A., Keating, K., Auken, E., 2015. A review of the principles and applications of the NMR technique for near-surface characterization. *Surv. Geophys.* 36 (1), 27–85. <https://doi.org/10.1007/s10712-014-9304-0>.
- Bogenes, T., Chappel, S., Krolkowski, C., 2003. Kapunda, heritage and tourism. *CAUTHE 2003: Riding the Wave of Tourism and Hospitality Research*, p. 1161.
- Boucher, M., et al., 2012. Constraining groundwater modeling with magnetic resonance soundings. *Ground Water* 50 (5), 775–784. <https://doi.org/10.1111/j.1745-6584.2011.00891.x>.
- Brunner, P., Hendricks Franssen, H.J., Kgotlhang, L., Bauer-Gottwein, P., Kinzelbach, W., 2006. How can remote sensing contribute in groundwater modeling? *Hydrogeol. J.* 15 (1), 5–18. <https://doi.org/10.1007/s10040-006-0127-z>.
- Bureau of Meteorology, 2020. Climate Statistics for Kapunda (023307). http://www.bom.gov.au/climate/averages/tables/cw_023307.shtml.
- Carr, H.Y., Purcell, E.M., 1954. Effects of diffusion on free precession in nuclear magnetic resonance experiments. *Phys. Rev.* 94 (3), 630–638. <https://doi.org/10.1103/PhysRev.94.630>.
- Chen, Y., Oliver, D.S., 2013. Levenberg–Marquardt forms of the iterative ensemble smoother for efficient history matching and uncertainty quantification. *Comput. Geosci.* 17 (4), 689–703.
- Christensen, N.K., Ferre, T.P.A., Fiandaca, G., Christensen, S., 2017. Voxel inversion of airborne electromagnetic data for improved groundwater model construction and prediction accuracy. *Hydrol. Earth Syst. Sci.* 21 (2), 1321–1337. <https://doi.org/10.5194/hess-21-1321-2017>.
- Craig, J.R., Ramadhan, M., Muffels, C., 2020. A particle tracking algorithm for arbitrary unstructured grids. *Groundwater* 58 (1), 19–26. <https://doi.org/10.1111/gwat.12894>.
- Davies, P.J., Crosbie, R.S., 2018. Mapping the spatial distribution of chloride deposition across Australia. *J. Hydrol.* 561, 76–88. <https://doi.org/10.1016/j.jhydrol.2018.03.051>.
- Doherty, J., 2003. Ground water model calibration using pilot points and regularization. *Ground Water* 41 (2), 170.
- Doherty, J., Simmons, C.T., 2013. Groundwater modelling in decision support: reflections on a unified conceptual framework. *Hydrogeol. J.* 21 (7), 1531–1537. <https://doi.org/10.1007/s10040-013-1027-7>.
- Doherty, J., Brebber, L., Whyte, P., 1994. *PEST: Model-Independent Parameter Estimation*, Vol. 122. Watermark Computing, Corinda, Australia, p. 336.
- ECHA, 1999. Biodegradation of Methanesulphonic Acid in Water: Screening Tests, Finland. <https://echa.europa.eu/registration-dossier/-/registered-dossier/14198/5/3/2>.
- Everett, M.E., 2013. *Near-Surface Applied Geophysics*. Cambridge University Press.
- Garcia, X., Jones, A.G., 2002. Atmospheric sources for audio-magnetotelluric (AMT) sounding. *GEOPHYSICS* 67 (2), 448–458. <https://doi.org/10.1190/1.1468604>.
- Hanke, M., 1997. A regularizing Levenberg-Marquardt scheme, with applications to inverse groundwater filtration problems. *Inverse Probl.* 13 (1), 79–95. <https://doi.org/10.1088/0266-5611/13/1/007>.
- Harrington, G.A., Gardner, W.P., Munday, T.J., 2014. Tracking groundwater discharge to a large river using tracers and geophysics. *Groundwater* 52 (6), 837–852. <https://doi.org/10.1111/gwat.12124>.
- Herckenrath, D., Fiandaca, G., Auken, E., Bauer-Gottwein, P., 2013. Sequential and joint hydrogeophysical inversion using a field-scale groundwater model with ERT and TDEM data. *Hydrol. Earth Syst. Sci.* 17 (10), 4043.
- Hidalgo, T., Kuhar, L., Beinlich, A., Putnis, A., 2019. Kinetics and mineralogical analysis of copper dissolution from a bornite/chalcopyrite composite sample in ferric chloride and methanesulfonic-acid solutions. *Hydrometallurgy* 188, 140–156. <https://doi.org/10.1016/j.hydromet.2019.06.009>.
- Hidalgo, T., Verrall, M., Beinlich, A., Kuhar, L., Putnis, A., 2020. Replacement reactions of copper sulphides at moderate temperature in acidic solutions. *Ore Geol. Rev.* 123, 103569. <https://doi.org/10.1016/j.oregeorev.2020.103569>.
- Hunt, R.J., Zheng, C.M., 2012. The current state of modeling. *Ground Water* 50 (3), 329–333. <https://doi.org/10.1111/j.1745-6584.2012.00936.x>.
- Jain, A.K., 2010. Data clustering: 50 years beyond K-means. *Pattern Recognit. Lett.* 31 (8), 651–666.
- Jeuken, B., Magarey, P., 2017. Kapunda Copper Project - Baseline Hydrogeological Assessment. *Groundwater Science*, Adelaide.
- Kelbert, A., Meqbel, N., Egbert, G.D., Tandon, K., 2014. ModEM: a modular system for inversion of electromagnetic geophysical data. *Comput. Geosci.* 66, 40–53. <https://doi.org/10.1016/j.cageo.2014.01.010>.
- Lambert, I.B., Donnelly, T.H., Rowlands, N.J., 1980. Genesis of upper proterozoic stratabound copper mineralization, Kapunda, South Australia. *Miner. Depos.* 15 (1), 1–18. <https://doi.org/10.1007/BF00202840>.
- Lamontagne, S., Kirby, J., Johnston, C., 2020. Groundwater – Surface Water Connectivity in a Chain-of-ponds Semiarid River. Manuscript submitted for publication.
- Legchenko, A., Baltassat, J.M., Beauce, A., Bernard, J., 2002. Nuclear magnetic resonance as a geophysical tool for hydrogeologists. *J. Appl. Geophys.* 50 (1–2), 21–46. [https://doi.org/10.1016/s0926-9851\(02\)00128-3](https://doi.org/10.1016/s0926-9851(02)00128-3).
- Li, C., Cranswick, R.H., 2016. Barossa PWRA Groundwater Resource Capacity: Numerical Groundwater Flow Modelling. DEWNR Technical Report 2016/05, Adelaide.
- Logan, J., 1964. Estimating transmissibility from routine production tests of water wells. *Groundwater* 2 (1), 35–37.
- Long, J., Remer, J., Wilson, C., Witherspoon, P., 1982. Porous media equivalents for networks of discontinuous fractures. *Water Resour. Res.* 18 (3), 645–658.
- Marker, P.A., et al., 2015. Performance evaluation of groundwater model hydrostratigraphy from airborne electromagnetic data and lithological borehole logs. *Hydrol. Earth Syst. Sci.* 19 (9), 3875–3890. <https://doi.org/10.5194/hess-19-3875-2015>.
- Meiboom, S., Gill, D., 1958. Modified spin-echo method for measuring nuclear relaxation times. *Rev. Sci. Instrum.* 29 (8), 688–691.
- Merrick, D., 2016. *AlgoMesh User Guide*, HydroAlgorithmics, Australian Capital Territory.
- Nirola, R., Megharaj, M., Aryal, R., Naidu, R., 2016. Screening of metal uptake by plant colonizers growing on abandoned copper mine in Kapunda, South Australia. *Int. J. Phytoremediation* 18 (4), 399–405. <https://doi.org/10.1080/15226514.2015.1109599>.
- Panday, S., Langevin, C.D., Niswonger, R.G., Ibaraki, M., Hughes, J.D., 2017. MODFLOW-USG Version 1.4.00: an Unstructured Grid Version of MODFLOW for Simulating Groundwater Flow and Tightly Coupled Processes Using a Control Volume Finite-difference Formulation. U.S. Geological Survey, United States. <https://doi.org/10.5066/F7R20ZFJ>.
- Poeter, E.P., Hill, M.C., Lu, D., Tiedeman, C., Mehl, S.W., 2014. UCODE2014, With New Capabilities to Define Parameters Unique to Predictions, Calculate Weights Using Simulated Values, Estimate Parameters With SVD, Evaluate Uncertainty With MCMC, and More. Integrated Groundwater Modeling Center (IGWMC), of the Colorado School of Mines.
- Purvanche, D.T., Andricevic, R., 2000. On the electrical-hydraulic conductivity correlation in aquifers. *Water Resour. Res.* 36 (10), 2905–2913. <https://doi.org/10.1029/2000wr900165>.
- Rau, G.C., et al., 2019. Error in hydraulic head and gradient time-series measurements: a quantitative appraisal. *Hydrol. Earth Syst. Sci.* 23 (9).
- Sinclair, L., Thompson, J., 2015. In situ leaching of copper: challenges and future prospects. *Hydrometallurgy* 157, 306–324.
- Slater, L., 2007. Near surface electrical characterization of hydraulic conductivity: from petrophysical properties to aquifer geometries—a review. *Surv. Geophys.* 28 (2–3), 169–197. <https://doi.org/10.1007/s10712-007-9022-y>.
- Spies, B.R., 1989. Depth of investigation in electromagnetic sounding methods. *GEOPHYSICS* 54 (7), 872–888. <https://doi.org/10.1190/1.1442716>.
- Vozoff, K., 1991. The magnetotelluric method, electromagnetic methods in applied geophysics: volume 2, application, parts a and B. *Soc. Exp. Geophys.* 641–712.
- Wagner, A.M., 2007. Using Geophysical Constraints To Determine Groundwater Travel Times, Seafloor Arrival Locations, And Saltwater Concentrations For Transition Zone Depths At Underground Nuclear Detonations On Amchitka Island.
- Welter, D.E., White, J.T., Hunt, R.J., Doherty, J.E., 2015. Approaches in Highly Parameterized Inversion—PEST++ Version 3, a Parameter ESTimation and Uncertainty Analysis Software Suite Optimized for Large Environmental Models. US Geological Survey, pp. 2328–7055.
- White, J.T., 2018. A model-independent iterative ensemble smoother for efficient history-matching and uncertainty quantification in very high dimensions. *Environ. Model. Softw.* 109, 191–201. <https://doi.org/10.1016/j.envsoft.2018.06.009>.
- Wood, W.W., 1999. Use and misuse of the chloride-mass balance method in estimating ground water recharge. *Ground Water* 37 (1), 2–5.